Pressure-induced phase transitions in the CdCr2Se4 spinel

I. Efthimiopoulos, Z. T. Y. Liu, M. Kucway, S. V. Khare, P. Sarin, Vladimir Tsurkan, Alois Loidl, Y. Wang

Angaben zur Veröffentlichung / Publication details:

Efthimiopoulos, I., Z. T. Y. Liu, M. Kucway, S. V. Khare, P. Sarin, Vladimir Tsurkan, Alois Loidl, and Y. Wang. 2016. "Pressure-induced phase transitions in the CdCr2Se4 spinel." *Physical Review B* 94 (17): 174106. https://doi.org/10.1103/physrevb.94.174106.

Pressure-induced phase transitions in the $CdCr_2Se_4$ spinel

I. Efthimiopoulos,[1,2] Z. T. Y. Liu,[3] M. Kucway,[1] S. V. Khare,[3] P. Sarin,[4] V. Tsurkan,[5,6] A. Loidl,[6] and Y. Wang[1,*]

[1]*Department of Physics, Oakland University, Rochester, Michigan 48309, USA*

[2]*Deutsches GeoForschungsZentrum (GFZ), Section 4.3, Telegrafenberg, 14473, Potsdam, Germany*

[3]*Department of Physics and Astronomy, University of Toledo, Toledo, Ohio 43606, USA*

[4]*School of Materials Science and Engineering, Oklahoma State University, Tulsa, Oklahoma 74106, USA*

[5]*Institute of Applied Physics, Academy of Sciences of Moldova, MD-2028 Chisinau, Republic of Moldova*

[6]*Experimental Physics V, Center for Electronic Correlations and Magnetism, Institute of Physics, University of Augsburg, D-86159 Augsburg, Germany*

(Received 17 August 2016; revised manuscript received 17 October 2016; published 14 November 2016)

We have conducted high-pressure x-ray diffraction and Raman spectroscopic studies on the $CdCr_2Se_4$ spinel at room temperature up to 42 GPa. We have resolved three structural transitions up to 42 GPa, i.e., the starting $Fd\bar{3}m$ phase transforms at ∼11 GPa into a tetragonal $I4_1/amd$ structure, an orthorhombic distortion was observed at ∼15 GPa, whereas structural disorder initiates beyond 25 GPa. Our *ab initio* density functional theory studies successfully reproduced the observed crystalline-to-crystalline structural transitions. In addition, our calculations propose an antiferromagnetic ordering as a potential magnetic ground state for the high-pressure tetragonal and orthorhombic modifications, compared with the starting ferromagnetic phase. Furthermore, the computational results indicate that all phases remain insulating in their stability pressure range, with a direct-to-indirect band gap transition for the $Fd\bar{3}m$ phase taking place at 5 GPa. We attempted also to offer an explanation behind the *peculiar* first-order character of the $Fd\bar{3}m$(cubic) → $I4_1/amd$ (tetragonal) transition observed for several relevant Cr spinels, i.e., the sizeable volume change at the transition point, which is not expected from space group symmetry considerations. We detected a clear correlation between the cubic-tetragonal transition pressures and the next-nearest-neighbor magnetic exchange interactions for the Cr-bearing sulfide and selenide members, a strong indication that the cubic-tetragonal transitions in these systems are principally governed by magnetic effects.

DOI: 10.1103/PhysRevB.94.174106

I. INTRODUCTION

The series of Cr-based ACr_2X_4 spinels with nonmagnetic A cations (A^{2+} = Zn, Cd, Hg; X^{2-} = O, S, Se) presents a prototype system for studying magnetic interactions in solids [1–3]. The spinel structure (space group [SG] $Fd\bar{3}m$, Z = 8; Fig. 1) is composed of edge-sharing CrX_6 octahedral and "isolated" AX_4 tetrahedral units. The magnetic Cr^{3+} cations with half-filled outer 3d t_{2g} orbitals, reside in a pyrochlore sublattice, i.e. form a network of corner-sharing tetrahedra (Fig. 1). This geometrical arrangement of the magnetic cations leads to substantial magnetic frustration, with the realization of diverse magnetic ground states [4].

The close connection between the magnetic and the structural properties in these systems is well established [4–8]. In particular, the magnetic exchange interactions of these compounds can be divided into nearest-neighbor (nn) J and weaker next-nearest-neighbor (nnn) K interactions. Regarding the former, the J interactions can be further subdivided into two parts: the direct antiferromagnetic (AFM) exchange between adjacent Cr^{3+} cations (J_1), and the indirect ferromagnetic (FM) Cr-X-Cr superexchange (J_2) [1,9–11]. The J_1 parameter dominates the magnetic interactions of the $ACrO_4$ oxides due the smaller Cr-Cr distances (proportional to the cubic lattice constant), thus leading to AFM ordering at low temperatures [3,4]. On the other hand, the larger Cr-Cr distances in the sulfide and selenide Cr spinels weaken the J_1 parameter, thus enhancing the contribution of the FM J_2 indirect interaction. Nevertheless, only $CdCr_2S_4$, $CdCr_2Se_4$, and $HgCr_2Se_4$ display a FM ground state, indicating the strong competition between FM and AFM interactions even for larger Cr-Cr separation [4]. As for the nnn K exchange interactions, their magnitude is relatively small compared with the J values in oxides but exhibit an increase for both sulfides and selenides [3,12].

Application of external pressure has been shown to tune the magnetic exchange interactions in Cr spinels effectively [13–17]. The straightforward effect of compression is the reduction of the Cr-Cr distances, which in turn causes the enhancement of the AFM J_1 interactions over the FM J_2 ones. Besides tuning the magnetic interactions, pressure can also lead to structural [18–23], electronic [21,24,25], and even magnetic [21] phase transitions in these compounds, often interrelated to each other.

Recently, we have observed diverse pressure-induced structural behavior in two Cr-selenide spinels, i.e., $ZnCr_2Se_4$ and $HgCr_2Se_4$. The former transforms from the starting $Fd\bar{3}m$ structure into a $CrMo_2S_4$-type phase at about 17 GPa [18], with mid-infrared reflectance [26], Raman spectroscopy, and *ab initio* density functional theory (DFT) methods indicating a concomitant insulator-metal transition upon the structural modification. On the other hand, $HgCr_2Se_4$ exhibits a $Fd\bar{3}m$-$I4_1/amd$ transition at 15 GPa, with further compression leading to structural disorder beyond 21 GPa [19]. Interestingly, an insulator-metal transition was predicted close to the cubic-tetragonal transition [24]. Given this structural divergence between $ZnCr_2Se_4$ and $HgCr_2Se_4$, resolving the high-pressure structural behavior of the "intermediate" (in

*Corresponding author: ywang235@oakland.edu

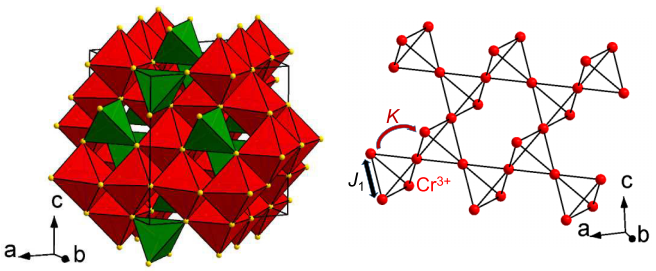

FIG. 1. Polyhedral representation of the spinel structure (SG $Fd\bar{3}m$, $Z = 8$, left). The green tetrahedra correspond to $CdSe_4$ units, whereas the red octahedra represent the $CrSe_6$ cages, with the Cd and Cr cations residing in the respective polyhedral units. The Se ions are displayed as yellow spheres. The corner-sharing tetrahedral pyrochlore network formed by the magnetic Cr^{3+} cations is also shown (right). The exchange paths J_1 and K are indicated.

terms of size) $CdCr_2Se_4$ compound becomes imperative for clarifying the pressure-induced structural systematics in these materials.

At ambient pressure, $CdCr_2Se_4$ is a FM semiconductor with FM ordering temperature $T_C = 130$ K [4] and band gap $E_g = 1.3$ eV (room temperature [RT] value) [27]. A red shift of E_g was detected below T_C [27], but without any apparent complementary structural effect [5,28]. As for its high-pressure behavior, a previous x-ray diffraction (XRD) investigation up to 18 GPa at ambient temperature showed that $CdCr_2Se_4$ undergoes a second-order structural transition into a tetragonal phase at ∼10 GPa; no space group was assigned, however [29]. In addition, high-pressure electron paramagnetic resonance (EPR) studies indicated substantial changes in the magnetic exchange interactions up to 8 GPa (the maximum pressure reached in the experiment) [16]. Finally, a monoclinic Cr_3S_4-type superstructure was also reported under combined high-pressure and high-temperature conditions (e.g., at 4 GPa and ∼770 K) [30]; this reaction was estimated to take place at a transition pressure $P_{Tr} = 7$ GPa at RT, which was not observed experimentally [29].

Having this rich high-pressure background as a guide, and given the aforementioned structural diversity of $ZnCr_2Se_4$ [18] and $HgCr_2Se_4$ [19], we have extended the high-pressure structural investigations of $CdCr_2Se_4$ up to 42 GPa at ambient temperature. Unlike the previous XRD report [29], our high-pressure Raman spectroscopic and XRD investigations revealed three successive structural transitions at ∼11 GPa (tetragonal $I4_1/amd$ phase), ∼15 GPa (orthorhombic distortion), and structural disorder initiating beyond 25 GPa. Our *ab initio* DFT studies successfully reproduced the first two structural transitions. In addition, our calculations confirmed that both of the high-pressure tetragonal and orthorhombic $CdCr_2Se_4$ phases exhibit AFM ordering as the most stable magnetic ground state, whereas all structures remain insulating throughout their experimental stability pressure range.

II. EXPERIMENTAL AND COMPUTATIONAL DETAILS

Details of the sample synthesis have been reported elsewhere [31]. Pressure was generated with a rhenium-gasketed diamond anvil cell (DAC), equipped with a set of diamonds with 300 μm culet diameter. The ruby luminescence method was employed for pressure calibration [32].

High-pressure Raman experiments at room temperature were conducted on single-crystalline $CdCr_2Se_4$ samples with a solid-state laser ($\lambda = 532$ nm) coupled to a single-stage Andor S500i Raman spectrometer. Both helium and a mixture of methanol-ethanol-water (M/E/W) 16:3:1 served as pressure-transmitting media (PTMs) in separate runs, yielding almost identical results. The Raman spectra were calibrated with a Hg lamp.

The angle-resolved high-pressure powder XRD measurements at room temperature were performed at the 16BM-D beamline of the High Pressure Collaborative Access Team (HPCAT), at the Advanved Photon Source (APS) of Argonne National Laboratory (ANL). The incident monochromatic x-ray beam energy was $E = 29.2$ keV ($\lambda = 0.4246$ Å), and the sample detector distance was 328 mm. The measured XRD diffractograms were processed with the FIT2D software [33]. Refinements were performed using the GSAS+EXPGUI software packages [34,35]. The *P-V* data were fitted with a Birch-Murnaghan equation of state (B-M EoS) [36]. Helium served as the PTM.

Density functional theory computations were performed with the Vienna *Ab initio* Simulation Package (VASP) [37–40]. The projector-augmented wave (PAW) method [41,42] and generalized gradient approximation (GGA) parameterized by Purdew, Burke, and Ernzerhoff (PBE) [43,44] were used. In terms of electronic configurations, we selected the potentials of Cd, Cr_pv, and Se, where "_pv" specifies the inclusion of semi-core p electrons. The plane wave energy cutoff was chosen to be 280 eV, and the k-point meshes were created with k points per reciprocal atom (KPPRA) of 1000. Gaussian smearing was used with a sigma value as small as 0.01 eV. The convergence criterion was set to 10^{-5} eV in energy during the electronic iterations. For structural optimization, the cell shape and atomic positions were allowed to relax until stress was minimized and force on any atom was below 0.01 eV/Å, similar to earlier papers [45–51]. The pressure dependence was determined by selecting a few volume points covering the equilibrium volumes corresponding to a range of 0–30 GPa, optimizing the structures at those points and fitting the total energy vs volume to a B-M EoS [36]. Then the pressure of each volume was obtained from the $P(V)$ formulation of the same EoS. Since the band gap E_g values are sensitive to exchange-correlation functionals and DFT calculations tend to underestimate them [52,53], the electronic band structure calculations were performed with the Heyd-Scuseria-Ernzerhof (HSE) hybrid functional [54,55] with the range separation parameter set to 0.2 (HSE06) in order to ensure closer agreement with the experimental E_g values.

III. RESULTS AND DISCUSSION

A. High-pressure Raman investigation of $CdCr_2Se_4$

As a first step for resolving the high-pressure structural behavior of $CdCr_2Se_4$, we have performed Raman spectroscopic investigations (Fig. 2). At ambient conditions, we could observe all of the expected $Fd\bar{3}m$ Raman-active modes [56,57]. Upon increasing pressure, the $Fd\bar{3}m$ Raman features

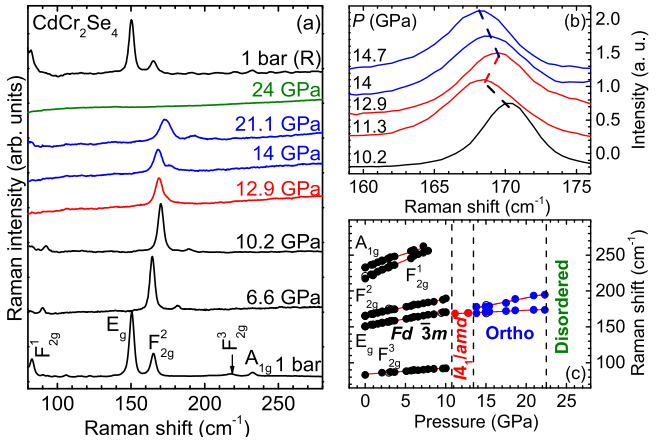

FIG. 2. (a) Selected Raman spectra of $CdCr_2Se_4$ at various pressures ($\lambda = 532$ nm, $T = 300$ K). The black, red, blue, and green spectra correspond to the $Fd\bar{3}m$, $I4_1/amd$, orthorhombic, and disordered phases, respectively. The spectra are presented as measured; notice the overall Raman intensity reduction at ~13 GPa. (b) Enhanced view of the E_g bending mode in the vicinity of the two successive phase transitions between 11 and 15 GPa. The spectra have been normalized to facilitate direct comparison. (c) Raman mode frequency evolution as a function of pressure for the various $CdCr_2Se_4$ phases. The vertical dashed lines represent the onset of the transitions.

could be followed up to 10 GPa. The respective Raman mode pressure coefficients and mode Grüneisen parameters γ_i of $CdCr_2Se_4$ are very similar to those of other Cr-based spinels [18–20] (Table I). We note that the $Fd\bar{3}m$ γ_i values have been calculated with the revised formula for polyatomic structures, as proposed by Hofmeister *et al.* [58].

At ~11 GPa we noticed an abrupt frequency downshift of the most intense E_g mode, which corresponds to a Se bending motion [59], as well as an overall Raman intensity reduction in our spectra (Fig. 2). Both of these observations lie in excellent agreement with the results of the former XRD study, which revealed a cubic-tetragonal transition close to 10 GPa [29]. We also mention that the Raman intensity drop appears to be a general feature of the Cr-bearing chalcogenide spinels upon adopting a tetragonal structure [19,20].

Increasing pressure further leads to another frequency downshift of the tetragonal E_g mode "descendant" at 14 GPa, as well as to the appearance of an additional feature at 176 cm^{-1} (Fig. 2). We interpret this behavior as a phase transition of the tetragonal $CdCr_2Se_4$ modification, which was not detected in the earlier XRD investigation [29]. This second high-pressure phase could be followed up to ~23 GPa; our Raman spectra become rather featureless beyond that pressure, hinting at yet another structural transition [Fig. 2(a)]. The disapperance of the Raman features above 23 GPa can be accounted for by (a) the adoption of a high-symmetry Raman-inactive phase, (b) structural disorder [60], and/or (c) an insulator-metal transition [61]. Our XRD study points to structural disorder as the reason behind the vanishing of Raman activity above 23 GPa, as we discuss below. Finally, the starting $Fd\bar{3}m$ phase could be recovered upon decompression at ~9.5 GPa; the reversibility of the original structure seems to be another general feature of Cr spinels [18–20].

B. Structure of $CdCr_2Se_4$ under pressure: XRD results

Selected XRD patterns of $CdCr_2Se_4$ are presented in Fig. 3(a). We can observe that the starting $Fd\bar{3}m$ phase persists up to 9.2 GPa. Several new Bragg peaks appear at the 11.6 GPa pattern, clearly indicating the onset of a structural transition at that pressure [Fig. 3(a)]. The new Bragg features dominated the XRD spectra at 12 GPa already, indicating the completion of the structural transformation. This high-pressure phase could be indexed with a tetragonal SG $I4_1/amd$ structure ($Z = 4$), similar to the first high-pressure phase of $HgCr_2Se_4$ [19] [Fig. 3(b)]. Upon increasing pressure at 15.4 GPa, however, the tetragonal phase could no longer provide a satisfactory model for our XRD patterns. Considering an orthorhombic distortion of the tetragonal cell, on the other hand, yielded excellent fittings of our XRD diffractograms beyond 15.4 GPa [Fig. 3(b)]. Further compression revealed signs of structural disorder initiating at 25 GPa, as revealed by the gradual Bragg peak broadening above that pressure (see Supplemental Material [62]); the XRD pattern collected at 35 GPa is composed of a sharp band located at ~10°, sitting on an extremely broad background [Fig. 3(a)]. Upon

TABLE I. Assignment [56,57], frequencies, pressure coefficients, and the mode Grüneisen parameters γ_i of the Raman-active modes of $CdCr_2Se_4$. The mode pressure dependence is described by the relation $\omega(P) = \omega_{Tr} + \alpha P_{Tr}$, where the frequency ω_{Tr} is in cm^{-1} (evaluated at the transition pressure point P_{Tr}) and P_{Tr} is in GPa. The mode Grüneisen parameters γ_i are determined from the relation: $\gamma_i = (B_{Tr}/\omega_{iTr}) \times (\partial\omega_i/\partial P)$. We employ the $B_{Tr} = 117(6)$ GPa and 57(3) GPa values for the $CrSe_6$- and $CdSe_4$-related $Fd\bar{3}m$ vibrations, respectively (see Supplemental Material [62]). Since the Raman mode assignment for the high-pressure $I4_1/amd$ and orthorhombic (Orthorh.) phases is not known, we use the "bulk" $B_{Tr} = 90(2)$ GPa ($I4_1/amd$) and $B_{Tr} = 100(1)$ GPa (orthorhombic) values, as obtained from the respective P-V data EoS fittings in our XRD study.

Phase	Assignment	P_{Tr} (GPa)	ω_{Tr} (cm^{-1})	$\partial\omega/\partial P$ (cm^{-1}/GPa)	γ_i
$Fd\bar{3}m$	$F^3{}_{2g}$ ($CdSe_4$)	1 bar	84	0.9	0.61
	E_g ($CrSe_6$)		151	2	1.55
	$F^2{}_{2g}$ ($CrSe_6$)		166	2.3	1.62
	$F^1{}_{2g}$ ($CrSe_6$)		219	4.9	2.62
	A_{1g} ($CrSe_6$)		234	3.6	1.8
$I4_1/amd$		11.3	169	0.5	0.27
Orthorh.		15.4	171	0.5	0.29
			179	2.2	1.23

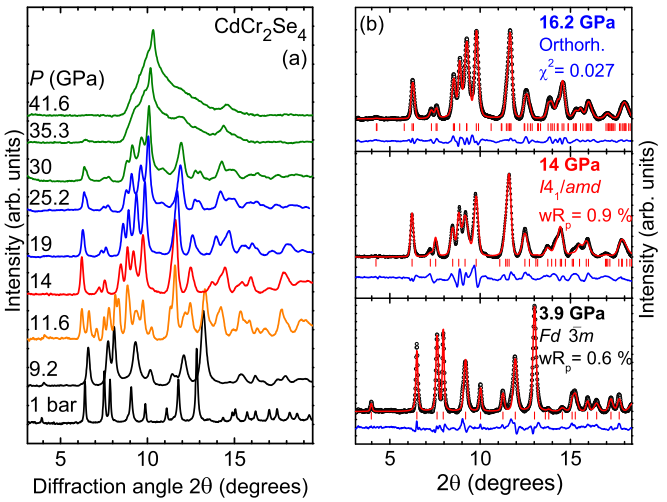

FIG. 3. (a) XRD patterns of $CdCr_2Se_4$ at selected pressures ($T = 300$ K, $\lambda = 0.4246$ Å). The various phases are indicated by different colors: black for $Fd\bar{3}m$, orange for coexistence, red for $I4_1/amd$, blue for orthorhombic, and green for disordered. Background has been subtracted for clarity. (b) Refinements of $CdCr_2Se_4$ XRD patterns at 3.9 GPa (Rietveld, bottom), 14 GPa (Rietveld, middle), and 16.2 GPa (Le Bail, top). Dots stand for the measured spectra, the red solid lines represent the best refinements, and their difference is drawn as blue lines. Vertical ticks mark the respective Bragg peak positions.

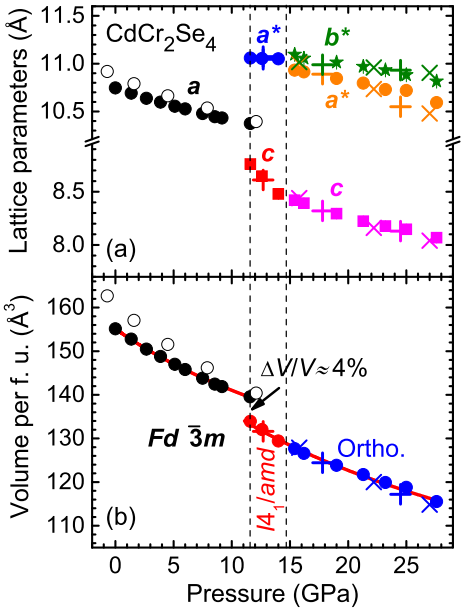

FIG. 4. (a) Lattice parameters and (b) unit cell volume per formula unit (f.u.) as a function of pressure for all phases of $CdCr_2Se_4$ (error bars lie within the symbols). The closed and open symbols correspond to experimental and DFT calculated data, respectively (○: cubic, +: AFM1, ×: AFM2, $a^* = \sqrt{2}a$, $b^* = \sqrt{2}b$; see Sec. C for descriptions of the AFM1 and AFM2 phases). The vertical dashed lines mark the structural transitions.

decompression, the original phase is partially recovered (see Supplemental Material [62]).

Generally, the transition pressures P_{Tr} of the $Fd\bar{3}m \rightarrow I4_1/amd$, the $I4_1/amd \rightarrow$ orthorhombic, and the orthorhombic $\rightarrow$ disorder transitions determined by our XRD study are in very good agreement with our Raman observations [Fig. 2(b)]. The minor deviations in the P_{Tr} can be accounted for by (a) the different PTMs employed in the two investigations [63,64] (we note that M/E/W remains hydrostatic up to ~10.5 GPa, whereas helium provides generally good hydrostatic conditions up to 40 GPa) [65] and (b) the different "sensitivity" of the two methods (Raman probes the structure on a local scale, whereas XRD serves more as a bulk probe of the lattice). Since the Raman investigations were performed with both PTMs and yielded almost identical results, we tend to attribute the small P_{Tr} differences in the more local nature of Raman spectroscopy (see, e.g., Ref. [66] for more details). We finally note that the structural disorder detected by XRD matches the vanishing of the Raman signal [Fig. 2(a)].

The quality of the obtained XRD diffractograms allowed for full Rietveld refinements of the $Fd\bar{3}m$ and the $I4_1/amd$ structures [Fig. 3(b)]. The refined parameters in each case were the lattice parameters, the atomic coordinates of Se (Cd and Cr reside in fixed positions for both structures; see Supplemental Material [62]), and the profile parameters of the Stephens peak function [67], whereas the background was modeled with a Chebyshev polynomial. Since the diffractograms showed textured rings, we employed a spherical harmonics correction [68] in order to account for the preferred orientation of the powder particles. All of the Rietveld refinements were performed with spherical harmonic orders of 6 and 8 (two and three refinable parameters, respectively) for the $Fd\bar{3}m$ phase and of 4 and 6 (three and five refinable parameters, respectively) for the $I4_1/amd$ high-pressure modification. The atomic coordinates from the two fits were found to be almost equal within the estimated uncertainties, and the results reported here [62] are the averages of these two refinements for each XRD pattern. We note that the estimated texture index from the spherical harmonics correction did not vary substantially with pressure; hence, the noticeable pressure-induced changes in the relative intensities of the Bragg peaks [especially for the $Fd\bar{3}m$ phase; Fig. 3(a)] arise mostly from the variation of the Se atomic position. The weighted residuals of the Rietveld fits wR_p and the reduced χ^2 parameters ("goodness of the fit") varied between 0.5–2.5% and 0.01–0.09 for all XRD refinements, respectively. We should finally mention that the isotropic atomic displacement parameters U_{iso} for the $Fd\bar{3}m$ phase were found to be pressure insensitive; hence, they were fixed to their refined ambient pressure values (see Supplemental Material [62]). On the other hand, attempts to refine the U_{iso} parameters for the $I4_1/amd$ phase resulted in either improbably small or negative values; consequently, we fixed these parameters to the ambient pressure $Fd\bar{3}m$ U_{iso} values as well. On the other hand, the significant number of overlapping Bragg peaks after the tetragonal-orthorhombic distortion above 15.4 GPa does not permit the determination of a unique orthorhombic space group; hence, only the lattice parameters could be extracted for this phase (see Supplemental Material [62]).

In Fig. 4 we present the lattice parameters and the respective P-V data for all phases of $CdCr_2Se_4$. Fitting of the experimental and calculated P-V data with B-M EoS [36] functions yielded the respective elastic parameters (Table II). In particular,

TABLE II. Elastic parameters (volume V_{Tr}, bulk modulus B_{Tr}, and the pressure derivative of bulk modulus B_{Tr}') for the various phases of $CdCr_2Se_4$, as obtained by a Birch-Murnaghan EoS [36] fitted to the measured P-V data. Each parameter is evaluated at the transition pressure point P_{Tr}. See Sec. C for descriptions of AFM1 and AFM2 phases. Exp. = experimental; NM = nonmagnetic.

Phase		P_{Tr} (GPa)	V_{Tr}/Z(Å^3)	B_{Tr} (GPa)	$B_{Tr'}$
$Fd\bar{3}m$	Exp.	1 bar	155.1(fixed)	81(2)	5.4(7)
	DFT (FM)		160.7	66.47	4.5
	Exp. [29]		155.1	103(1)	4(fixed)
	DFT (FM) [70]		147.8	80.2	5.85
	DFT (NM) [70]		139.6	92	4.59
$I4_1/amd$	Exp.	11.5	133.8(fixed)	90(2)	4(fixed)
	DFT (AFM1)		133.62	82.11	4.6
	DFT (AFM2)		134.81	81.26	3.5
Orthorh.	Exp.	15.4	127.7(fixed)	100(1)	4(fixed)
	DFT (AFM1)		127.56	99.87	4.6
	DFT (AFM2)		128.62	94.86	3.5

by keeping the respective starting volumes V_{Tr} for each phase fixed, we employed a third-order B-M EoS for the $Fd\bar{3}m$ phase and a (single) second-order B-M EoS for the high-pressure tetragonal and orthorhombic structures (the pressure derivative of the bulk modulus B' was fixed in the latter case). The order of the $Fd\bar{3}m$ B-M EoS fitting was determined from the plot of the Eulerian strain f_E as a function of the normalized pressure F [62]. Furthermore, our $Fd\bar{3}m$ bulk modulus B_0 is smaller compared with the B_0 determined in the previous high-pressure XRD study [29], with the discrepancy arising probably from the different experimental conditions, i.e., the PTM employed in each investigation.

Upon reaching the $Fd\bar{3}m$-$I4_1/amd$ transition, we see a sizeable volume decrease at the transition point (~4%) [Fig. 4(b)]. This volume drop was not detected in the previous investigation [29] but is consistent with the high-pressure behavior of several other Cr-based spinels which undergo similar transitions [19,20,22,23]. The first-order character of the cubic-tetragonal transition is unexpected from group symmetry considerations [69], since the SG $I4_1/amd$ is a direct subgroup of SG $Fd\bar{3}m$. Actually, the tetragonal unit cell can be easily derived from the cubic one, since the tetragonal c axis equals the cubic lattice parameter a_{cub}, whereas the tetragonal axis $a_{tetr} = a_{cub}/\sqrt{2}$ (note that we employ the normalized $a^* = a_{tetr}\sqrt{2}$ tetragonal lattice parameter in our discussion and graphs from now on, for direct comparison with the a_{cub}). In addition, the $I4_1/amd$ structure retains the same cationic coordination as the cubic phase (fourfold for Cd, sixfold for Cr).

Close comparison of our results with the previous XRD study [29] reveals that the reason behind the cubic-tetragonal ~4% volume drop is the smaller tetragonal axial ratio $c/a^* = 0.79$ at the transition point as determined here, compared with the larger $c/a^* = 0.91$ reported earlier. Additional insight can be gained from the behavior of the interatomic parameters throughout the $Fd\bar{3}m \rightarrow I4_1/amd$ transition. In Fig. 5 we present selected bond angles and bond lengths as a function of pressure. The Cr-Se-Cr bond angle, which serves as the pathway for the nn FM superexchange in the $Fd\bar{3}m$ phase, exhibits a marginal decrease against pressure [Fig. 5(a)]. This appears to be a common feature among Cr-based spinels [19,20,22,23]. Furthermore, all of the cation-anion bond distances decrease upon compression, with the Cd-Se bond being more compressible [Fig. 5(b)]. Upon passing into the $I4_1/amd$ phase, the Cr-Se-Cr, Cr-Se, and Cr-Cr parameters split into two distinct groups (as dictated by the tetragonal crystalline symmetry), i.e., into apical (along the c axis) and equatorial (parallel to the ab plane) components. The most interesting observation arises from the change in the shape of the $CrSe_6$ octahedra at the $Fd\bar{3}m$-$I4_1/amd$ transition, which become flattened along the apical direction (Fig. 5). The shortened Cr-Se, and subsequently Cr-Cr, bond distances along one direction imply significant changes in the respective magnetic exchange interactions at the cubic-tetragonal transition. As we will see in the next section, our DFT calculations have actually revealed substantial changes in the magnetic properties upon passing into the tetragonal structure.

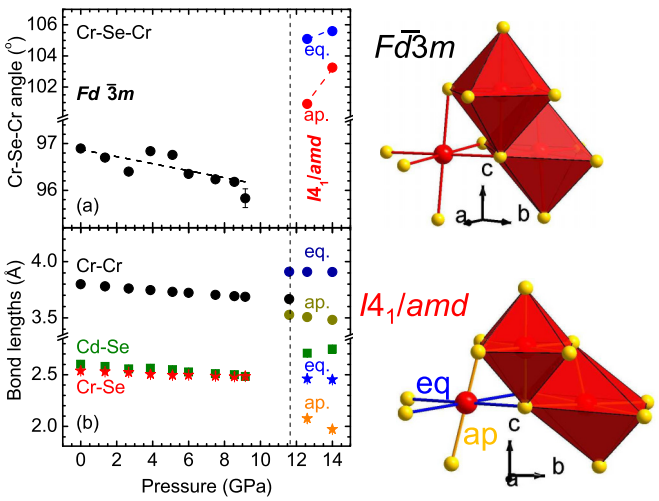

FIG. 5. (a) The Cr-Se-Cr bond angle and (b) selected bond lengths as a function of pressure for the $Fd\bar{3}m$ and the $I4_1/amd$ phases of $CdCr_2Se_4$. The vertical dashed line marks the structural transitions. The $CrSe_6$ octahedra for both phases are also shown for comparison. Abbreviations: eq = equatorial; ap = apical.

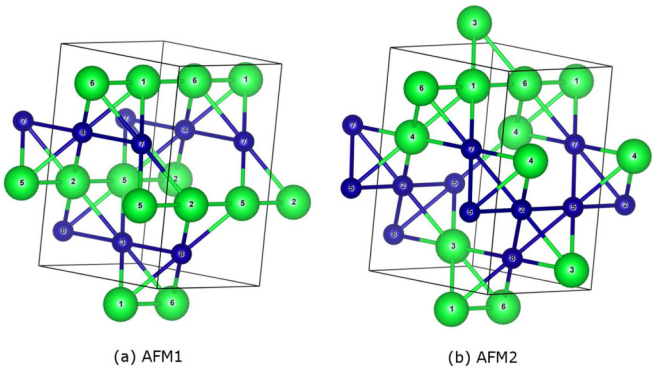

FIG. 6. The two different AFM configurations for the tetragonal phase of $CdCr_2Se_4$ considered in our calculations. (a) The AFM1 phase has an alternating layered construction of Cr^{3+} spins along the c axis. (b) The AFM2 modification exhibits an alternation of Cr^{3+} spins every two layers along the c axis, with one Cr^{3+} layer also showing intralayer alternation. The numbers 1–8 correspond to the different Cr ions employed for the construction of the tetragonal cell (see Supplemental Material [62]).

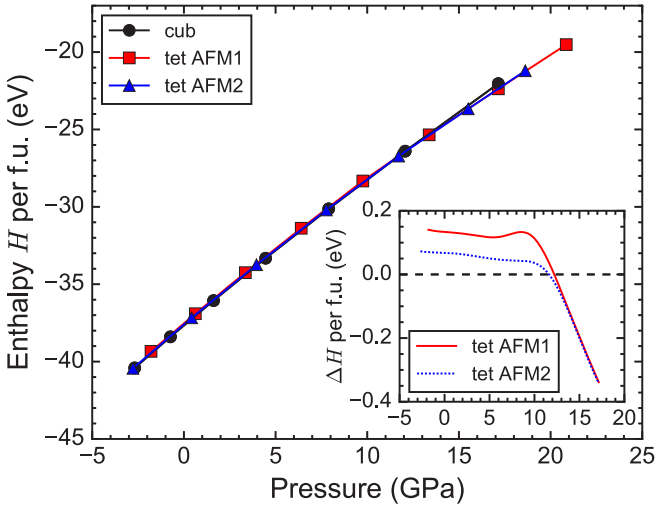

FIG. 7. The calculated enthalpies of the cubic FM (black) and the tetragonal AFM1 (red) and AFM2 (blue) phases as a function of pressure. Inset: the enthalpy difference between the tetragonal AFM1 and AFM2 phases and the cubic FM phase with respect to pressure. Enthalpy H is defined as $H(P) = E + PV$, and a phase is stable if it has a lower value of H.

As we already mentioned, the XRD patterns above 15.4 GPa could be modeled with an orthorhombic structure [Fig. 3(b)]. The obtained lattice parameters point to a small orthorhombic distortion of the tetragonal phase at this pressure ($b/a = 1.015$ at 15.4 GPa), which becomes more prominent upon further compression [Fig. 4(a)] (see Supplemental Material [62]). Since we could not detect any volume discontinuity at the transition point, we classify the tetragonal-orthorhombic transition as a second-order transition [Fig. 4(b)]. For this reason, we have employed the same second-order EoS fitting for both the tetragonal and orthorhombic phases.

Finally, the XRD patterns clearly show structural disorder of $CdCr_2Se_4$ at 35 GPa, similar to $HgCr_2Se_4$ [19]. By monitoring the Bragg peak width of the single orthorhombic peaks located at $2\theta \approx 9°$ and 9.3°, we managed to determine the onset of disorder close to 25 GPa (see Supplemental Material [62]), in very good agreement with the vanishing of the Raman signal [Fig. 2(a)]. Given that disordered states are frequently kinetically hindered structural transformations [71], we speculate that the disordered phase of $CdCr_2Se_4$ is a transient of a denser crystalline state, such as the high-pressure $CrMo_2S_4$-type modification of $ZnCr_2Se_4$ [18] or a Cr_3S_4-type structure [21,72] with sixfold coordination for both metal cations.

C. Magnetic and electronic properties of $CdCr_2Se_4$ under pressure

In order to examine the evolution of the magnetic and electronic properties of $CdCr_2Se_4$ throughout the pressure-induced structural transitions, we have conducted *ab initio* DFT calculations. We performed simulations for three phases of $CdCr_2Se_4$, i.e., the FM cubic spinel phase and two tetragonal AFM (AFM1 and AFM2) phases with different Cr^{3+} magnetic configurations. Illustrated in Fig. 6, the selected AFM phases are two of the many realized in the three-dimensional pyrochlore lattice. Attempts to employ a FM tetragonal phase resulted in a lattice equivalent to the FM cubic spinel structure, i.e., little c/a^* axial ratio deviation from 1 was observed. In addition, even though the b/a ratios of both AFM phases deviate from 1 beyond 15 GPa and become essentially orthorhombic (as we discuss below), we still use the notation "tetragonal" in our figures because of the gapless transition.

In order to examine the cubic-tetragonal transition from a theoretical standpoint, we have calculated and compared the enthalpies $H(P) = E + PV$ of the FM cubic phase and the two AFM tetragonal phases (Fig. 7). In the inset of Fig. 7 we can observe that both AFM phases become energetically favorable at 12 GPa. The calculated transition pressure lies in excellent agreement with our experimental observations (Figs. 2–4).

In Fig. 4 we plot the calculated cell parameters of the FM cubic and the two AFM tetragonal phases with respect to pressure against their experimental counterparts (see Supplemental Material [62]). The calculated cubic structural parameters exhibit a small deviation of ∼2% at low pressures, with this difference eliminated upon pressure increase. As a result, the calculated $Fd\bar{3}m$ bulk modulus shows an ∼20% smaller value compared with its experimental counterpart (Table II). As for the AFM tetragonal phases, the calculated lattice parameters are in excellent agreement with the experimental ones (Fig. 4). The tetragonal c/a^* axial ratios for both AFM phases remain close to 1 below 7 GPa, drop to ∼0.76 within the 7–12 GPa pressure range, and stay constant beyond that pressure (see Supplemental Material [62]). The detailed optimization process for the c/a^* ratios is included in the Supplemental Material [62]. Meanwhile, the calculated b/a axial ratios stay around 1 until ∼15 GPa, deviating above 1 beyond that pressure. In other words, both of the tetragonal AFM phases undergo orthorhombic distortions above 15 GPa, in excellent agreement with the experimental observations (Figs. 2–4). The calculated bulk moduli for the tetragonal and orthorhombic phases exhibit deviations of ∼9–10% and

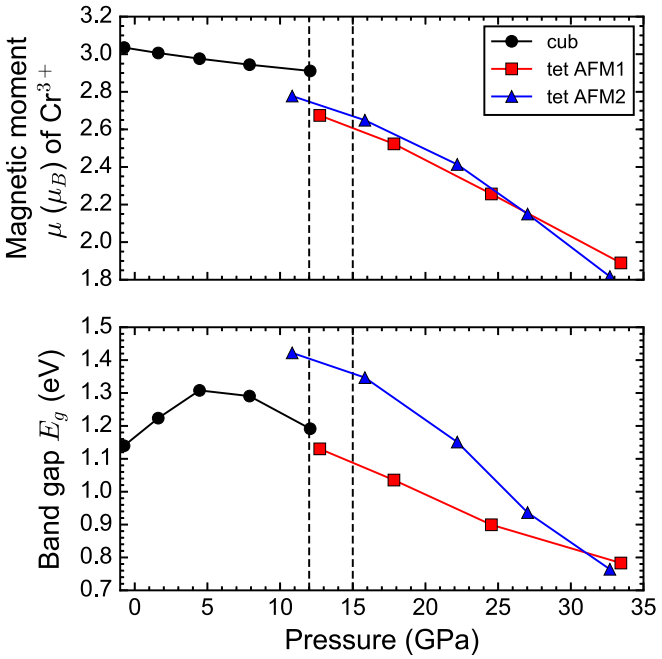

FIG. 8. The average magnetic moment μ of Cr^{3+} and electronic band gap E_g (with HSE functionals) for the FM cubic (○), and the tetragonal AFM1 (□) and AFM2 (△) phases with respect to pressure.

∼0.3–5% with respect to the experimental values, respectively (Table II), well within the range expected from DFT.

In Fig. 8 we plot the effect of pressure on the average magnetic moment μ of Cr^{3+} for the FM cubic and the AFM tetragonal phases. Upon increasing pressure, the μ values drop for all three phases. By passing into the orthorhombic phases above 15 GPa, the μ compressibilities for both AFM phases are further enhanced. Assuming that the two AFM modifications remain stable at higher pressures, a simple extrapolation of the existing curves yields a zero μ value either at 80 GPa (AFM1) or 63 GPa (AFM2).

As for the electronic band gap E_g calculated with HSE06 hybrid functionals (see Supplemental Material [62]), the FM cubic band gap at ambient pressure ($E_g^{calc} = 1.15$ eV, Fig. 9) agrees very well with the experimental value at the lowest recorded temperature ($E_g^{exp} = 1.16$ eV at 20 K) [27] and with previous DFT calculations [73]. Upon increasing pressure, the E_g values for the $Fd\bar{3}m$ phase increase in magnitude up to 5 GPa, whereas a decrease is observed within the 5–12 GPa pressure range, prior to the cubic-tetragonal transition (Fig. 8). The cause behind this E_g behavior can be attributed to the diverse pressure-induced evolution of the spin-up and spin-down states comprising the conduction band (CB) of the $Fd\bar{3}m$ phase (Fig. 9). In particular, the band gap is indirect from Γ to near X between 0–5 GPa; as pressure increases, the spin-up CB minimum near X shifts to higher energy, resulting in a slightly larger E_g. During this process, however, the spin-down CB states at Γ gradually descend energy-wise, and eventually move to lower energies compared with the original CB minimum near X beyond 5 GPa. Above that pressure, the band gap of $CdCr_2Se_4$ becomes direct at Γ; further compression leads to a steady decrease of the $Fd\bar{3}m$ E_g values. Such gradual pressure-induced E_g reduction is observed for both of the tetragonal (and orthorhombic) AFM1 and AFM2 high-pressure phases, but with different starting points (Fig. 8); the E_g values, though, do not drop to zero within the investigated pressure range, i.e., 0–35 GPa. A simple extrapolation of the existing curves yields zero E_g values either at 80 GPa ($dE_g/dP = -0.0165$ eV/GPa, AFM1) or 57 GPa ($dE_g/dP = -0.032$ eV/GPa, AFM2). This electronic behavior is rather different compared with other Cr spinels, where pressure-induced insulator-metal transitions at lower pressures are reported [18,21,24,25].

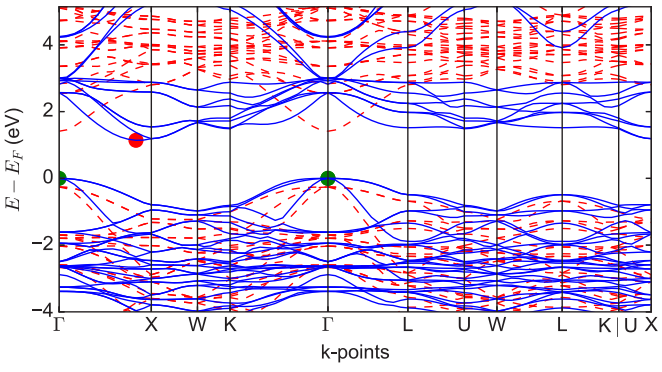

FIG. 9. Calculated band structure (with HSE06 hybrid functionals) of the $Fd\bar{3}m$ phase at zero pressure. The blue and red lines stand for spin-up and spin-down channels. The green and red points indicate the valence band maximum and conduction band minimum, respectively.

D. The puzzling $Fd\bar{3}m \rightarrow I4_1/amd$ first-order transition

As we mentioned earlier, the noticeable volume drop at the $Fd\bar{3}m \rightarrow I4_1/amd$ pressure-induced transition is unexpected from space group symmetry considerations, even though our observation is in line with the high-pressure behavior of several Cr-based spinels [19,20,22,23]. A pressure-activated Fe^{2+} orbitally driven Jahn-Teller effect, i.e., a lowering of the cubic symmetry to tetragonal due to a rearrangement of the outer Fe $3d$ orbitals, was proposed to account for the first-order character of the transition in $FeCr_2O_4$ [22]. We should mention here, however, that such pressure-induced activation of Jahn-Teller effects is quite rare in materials, since the effect of pressure is generally the suppression of Jahn-Teller distortions [74,75]. Given though that this type of Jahn-Teller distortion requires ions with degenerate electrons [76], this scenario cannot be applicable in the case of the orbitally inactive Cr^{3+} spinels such as $CdCr_2Se_4$. Even though a pressure-induced change in the valence state of Cr^{3+} toward, e.g., Cr^{2+} upon the $Fd\bar{3}m \rightarrow I4_1/amd$ transition could in principle "trigger" such a Jahn-Teller distortion, this would imply the delocalization of carriers from the Cr sites. In other words, the $Fd\bar{3}m \rightarrow I4_1/amd$ transition should be accompanied by an abrupt drop of both E_g and μ quantities, which is not supported by our calculations (Fig. 8).

On the other hand, the volume drop might originate from steric effects. In this case, the $Fd\bar{3}m$-$I4_1/amd$ transition pressure P_{Tr} should depend on the size of the involved ions. Such a relationship has been already proposed by Errandonea *et al.* [77] and was found to hold for several ternary compounds,

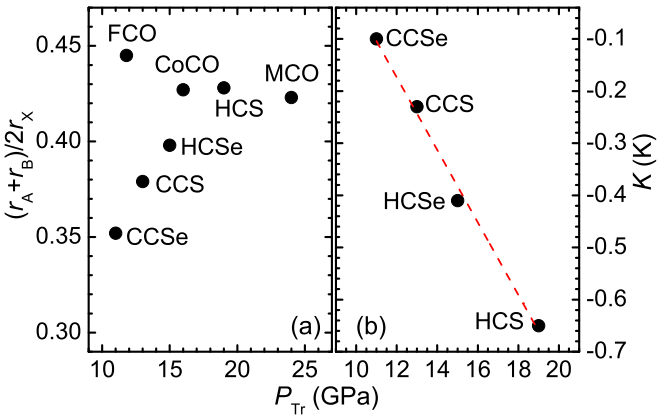

FIG. 10. Plot of (a) the ternary ionic radius ratio (see text) and (b) the nnn magnetic exchange interaction K against the cubic-tetragonal transition pressure P_{Tr}. Negative values stand for AFM interactions. For the compound abbreviations, see Table III.

including spinels and chalcopyrites. In particular, P_{Tr} was shown to be proportional to the ionic radius ratio $\frac{r_A+r_B}{2r_X}$, where r_A, r_B, and r_X stand for the ionic radii of the A, B, and X ions comprising the ternary materials. In Fig. 10(a) we plot the cubic-tetragonal transition pressures of various Cr-based spinels as a function of this ionic radius ratio, with the respective values listed in Table III. As we can observe, there is no apparent correlation between the two parameters.

On the other hand, the change of the $CdCr_2Se_4$ magnetic ordering from FM to AFM upon passing into the tetragonal phase as discussed in the previous section, clearly points to underlying magnetic effects at the $Fd\bar{3}m \rightarrow I4_1/amd$ transition. Actually, the pressure-induced evolution of the magnetic exchange interactions, as revealed by high-pressure EPR studies [16], reveals that the nn J and the nnn K interactions become almost equivalent at ~8 GPa, close to the structural transition. This observation indicates the important role of the nnn K interactions in $CdCr_2Se_4$, at least under these pressure conditions. Even though the respective magnetic exchange parameters as a function of pressure have not been reported for the rest of the relevant Cr spinels (Table III), examination of the nnn K values at ambient pressure reveals a straightforward trend between K and the transition pressures P_{Tr} for sulfides and selenides exhibiting the $Fd\bar{3}m \rightarrow I4_1/amd$ transition [Fig. 10(b)]. On the other hand, we could not detect a clear correlation between P_{Tr} and the nn J values (Table III). Interestingly, a similar correlation between nnn magnetic exchange interactions and the AFM-induced structural transitions in Cr-spinel oxides at ambient pressure was recently observed [78].

We should mention here that we have employed the nnn K values from the early calculations of Baltzer *et al.* [1] derived from the modeling of experimental magnetic susceptibility data. The same approach was employed in the high-pressure EPR study [16]. Even though more elaborate methods exist for determining magnetic exchange interactions in these systems [2,3], our main interest here was to uncover a possible link between structure and magnetism on a qualitative level. Note also that we have intentionally excluded the $FeCr_2O_4$, $CoCr_2O_4$, and $MgCr_2O_4$ compounds from the plot in Fig. 10(b), because (a) the next nearest neighbor magnetic exchange interactions of Cr oxospinels with magnetic A cations are not available [79–81] and (b) the K value of $MgCr_2O_4$ determined by the magnetic susceptibility data (but not with the Baltzer model) [12] is significantly different from that of sulfides and selenides, hindering any direct comparison.

Hence, we propose that the volume change at the cubic-tetragonal transition observed in several sulfide and selenide ACr_2X_4 spinels with nonmagnetic A cations (A^{2+} = Cd, Hg; X^{2-} = S, Se) arises due to the strong enhancement of the next nearest neighbor magnetic exchange interactions K upon sufficient compression. Such increase may lead to a strong competition between the nn J and nnn K interactions, resulting in first-order structural transitions toward lower symmery states (e.g., cubic-tetragonal) for relieving the built-up magnetic frustration [84,85]. In other words, we propose that the $Fd\bar{3}m \rightarrow I4_1/amd$ transition can be regarded as a *spin-driven Jahn-Teller transition* (and not orbitally driven, as in the case of $FeCr_2O_4$) [22]. Following our assumption, it might be that the tetragonal-orthorhombic distortion is also triggered by the competition of several energetically equivalent magnetic states, which can be "tuned" by moderate compression.

IV. CONCLUSIONS

We have conducted high-pressure XRD and Raman spectroscopic studies on the $CdCr_2Se_4$ cubic spinel at room temperature. Unlike the earlier XRD investigation [29], we have resolved three structural transitions up to 42 GPa, i.e., at ~11 GPa into a tetragonal $I4_1/amd$ phase (first order), at ~15 GPa into an orthorhombic distortion (second order), and

TABLE III. List of several Cr spinels exhibiting the $Fd\bar{3}m \rightarrow I4_1/amd$ transition along the respective cubic-tetragonal transition pressures P_{Tr}, their ionic radius ratios $\frac{r_A+r_B}{2r_X}$, and their nnn K interactions (negative for AFM).

Compound	P_{Tr} (GPa)	$(r_A + r_B)/2r_X$ [82]	J (K) [1]	K (K) [1]
$CdCr_2S_4$ (CCS) [83]	13	0.379	11.8	−0.23
$CdCr_2Se_4$ (CCSe)	11	0.352	14	−0.1
$HgCr_2S_4$ (HCS) [20]	19	0.428	13	−0.65
$HgCr_2Se_4$ (HCSe) [19]	15	0.398	15.8	−0.41
$FeCr_2O_4$ (FCO) [22]	11.8	0.445		
$CoCr_2O_4$ (CoCO) [81]	16	0.427		
$MgCr_2O_4$ (MCO) [23]	24	0.423		

structural disorder beyond 25 GPa. The structural behavior of $CdCr_2Se_4$ matches closer that of the $HgCr_2Se_4$ [19] and $HgCr_2S_4$ [20] spinels compared with $ZnCr_2Se_4$ [18].

Our *ab initio* DFT studies could reproduce the observed structural transitions successfully. In addition, our calculations predict that both of the high-pressure tetragonal and orthorhombic $CdCr_2Se_4$ modifications exhibit AFM ordering compared with the FM ordering of the starting cubic structure, whereas all phases remain insulating throughout the investigated pressure range, i.e., up to 35 GPa. We note, however, that a transition from an indirect-to-direct band gap semiconductor has been observed for the $Fd\bar{3}m$ phase at 5 GPa.

Finally, we attempted to offer an explanation behind the sizeable volume change at the $Fd\bar{3}m \rightarrow I4_1/amd$ pressure-induced transitions observed for several Cr spinels, which is unexpected from group symmetry considerations. An orbitally driven Jahn-Teller effect as the driving force behind this transition, as proposed earlier for $FeCr_2O_4$ [22], does not seem plausible for $CdCr_2Se_4$ with orbitally inactive Cr^{3+} cations. On the other hand, we have found a direct correlation between the cubic-tetragonal P_{Tr} and the next nearest neighbor magnetic exchange interactions for the sulfide and selenide members. Even though the lack of pressure-related data does not permit a more general discussion at the moment, it appears that the $Fd\bar{3}m \rightarrow I4_1/amd$ transition originates from spin-driven Jahn-Teller effects; i.e., the lowering of the crystalline symmetry and the accompanying volume reduction act as "pressure relief valves" for the built-up magnetic frustration caused by the strong competition of the FM and AFM interactions in this system prior to the cubic-tetragonal transition.

ACKNOWLEDGMENTS

We thank Dr. D. Popov for his assistance with the XRD measurements and Dr. S. Tkachev at GeoSoilEnviroCARS (GSECARS; Sector 13), APS-ANL, for his assistance with the DAC gas loading. Portions of this work were performed at HPCAT (Sector 16), APS-ANL. HPCAT operations are supported by the U.S. Department of Energy (DOE)–National Nuclear Security Administration (NNSA) under Award No. DE-NA0001974 and the DOE–Basic Energy Sciences (BES) under Award No. DE-FG02-99ER45775, with partial instrumentation funding by the National Science Foundation (NSF). This research used resources of the APS, a DOE Office of Science User Facility operated for the DOE Office of Science by ANL under Contract No. DE-AC02-06CH11357. Use of the Consortium for Materials Properties Research in Earth Sciences (COMPRES)–GSECARS gas loading system was supported by COMPRES under NSF Cooperative Agreement No. EAR 11-57758 and by GSECARS through NSF Grant No. EAR-1128799 and DOE Grant No. DE-FG02-94ER14466. We acknowledge use of computational resources from the Tandy Supercomputing Center and the Ohio Supercomputing Center [86]. We acknowledge support from the NSF Civil, Mechanical, and Manufacturing Innovation (CMMI) Grants No. 1234777 and 1629239. This research has been partially supported by the Deutsche Forschungsgemeinschaft (DFG) via the Transregional Collaborative Research Center TRR 80 (Augsburg-Munich). We are grateful to the Michigan Space Grant consortium and the Research Faculty Fellowship of Oakland University for supporting this research.

[1] P. K. Baltzer, P. J. Wojtowicz, M. Robbins, and E. Lopatin, Phys. Rev. **151**, 367 (1966).
[2] K. Dwight and N. Menyuk, Phys. Rev. **163**, 435 (1967).
[3] A. N. Yaresko, Phys. Rev. B **77**, 115106 (2008).
[4] T. Rudolf, C. Kant, F. Mayr, J. Hemberger, V. Tsurkan, and A. Loidl, New J. Phys. **9**, 76 (2007).
[5] H. Goebel, J. Magn. Magn. Mater. **3**, 143 (1976).
[6] K. Wakamura and T. Arai, J. Appl. Phys. **63**, 5824 (1988).
[7] J. Hemberger, T. Rudolf, H.-A. K. von Nidda, F. Mayr, A. Pimenov, V. Tsurkan, and A. Loidl, Phys. Rev. Lett. **97**, 087204 (2006).
[8] J. Hemberger, H.-A. Krug von Nidda, V. Tsurkan, and A. Loidl, Phys. Rev. Lett. **98**, 147203 (2007).
[9] J. B. Goodenough, Phys. Rev. **117**, 1442 (1960).
[10] J.B. Goodenough, J. Phys. Chem. Sol. **6**, 287 (1958).
[11] J. Kanamori, J. Phys. Chem. Sol. **10**, 87 (1959).
[12] C. Kant, J. Deisenhofer, V. Tsurkan, and A. Loidl, J. Phys. Conf. Ser. **200**, 032032 (2010).
[13] H. Ueda and Y. Ueda, Phys. Rev. B **77**, 224411 (2008).
[14] Y. Jo, J.-G. Park, H. C. Kim, W. Ratcliff II, and S.-W. Cheong, Phys. Rev. B **72**, 184421 (2005).
[15] T. Kanomata, K. Shirakawa, and T. Kaneko, J. Magn. Magnet. Mater. **54**, 1297 (1986).
[16] N. Sakai and J. H. Pifer, Phys. Rev. B **33**, 1875 (1986).
[17] V. C. Srivastava, J. Appl. Phys. **40**, 1017 (1969).
[18] I. Efthimiopoulos, Z. T. Y. Liu, S. V. Khare, P. Sarin, V. Tsurkan, A. Loidl, D. Popov, and Y. Wang, Phys. Rev. B **93**, 174103 (2016).
[19] I. Efthimiopoulos, A. Yaresko, V. Tsurkan, J. Deisenhofer, A. Loidl, C. Park, and Y. Wang, Appl. Phys. Lett. **104**, 011911 (2014).
[20] I. Efthimiopoulos, A. Yaresko, V. Tsurkan, J. Deisenhofer, A. Loidl, C. Park, and Y. Wang, Appl. Phys. Lett. **103**, 201908 (2013).
[21] Y. Amiel, G. K. Rozenberg, N. Nissim, A. Milner, M. P. Pasternak, M. Hanfland, and R. D. Taylor, Phys. Rev. B **84**, 224114 (2011).
[22] A. Kyono, S. A. Gramsch, T. Yamanaka, D. Ikuta, M. Ahart, B. O. Mysen, H. K. Mao, and R. J. Hemley, Phys. Chem. Miner. **39**, 131 (2012).
[23] W. Yong, S. Botis, S. R. Shieh, W. Shi, and A. C. Withers, Phys. Earth Planet. Inter. **196–197**, 75 (2012).
[24] S.-D. Guo and B.-G. Liu, J. Phys. Cond. Mat. **24**, 045502 (2012).
[25] P. Kistaiah, K. S. Murthy, and K. V. K. Rao, J. Less-Com. Met. **98**, L13 (1984).
[26] K. Rabia, L. Baldassarre, J. Deisenhofer, V. Tsurkan, and C. A. Kuntscher, Phys. Rev. B **89**, 125107 (2014).
[27] G. Harbeke and H. Pinch, Phys. Rev. Let. **17**, 1090 (1966).
[28] M. Tachibana, N. Taira, and H. Kawaji, Sol. St. Com. **151**, 1776 (2011).

[29] A. Waskowska, L. Gerward, J. StaunOlsen, and E. Malicka, J. Phys. Cond. Mat. **14**, 12423 (2002).
[30] M. D. Banus and M. C. Lavine, J. Sol. St. Chem. **1**, 109 (1969).
[31] I. Okonska-Kozlowska, E. Malicka, A. Waskowska, J. Heimann, and T. Mydlarz, J. Sol. St. Chem. **158**, 34 (2001).
[32] H. K. Mao, J. Xu, and P. Bell, J. Geophys. Res. **91**, 4673 (1986).
[33] A. Hammersley, S. Svensson, M. Hanfland, A. Fitch, and D. Hausermann, High Press. Res. **14**, 235 (1996).
[34] B. H. Toby, J. Appl. Crystallogr. **34**, 210 (2001).
[35] R. B. von Dreele and A. C. Larson, Los Alamos Natl. Lab. Rep. No. LAUR 86-748 (1994).
[36] F. Birch, Phys. Rev. **71**, 809 (1947).
[37] G. Kresse and J. Furthmuller, Comput. Mater. Sci. **6**, 15 (1996).
[38] G. Kresse and J. Furthmüller, Phys. Rev. B **54**, 11169 (1996).
[39] G. Kresse and J. Hafner, Phys. Rev. B **49**, 14251 (1994).
[40] G. Kresse and J. Hafner, Phys. Rev. B **47**, 558 (1993).
[41] P. E. Blöchl, Phys. Rev. B **50**, 17953 (1994).
[42] G. Kresse and D. Joubert, Phys. Rev. B **59**, 1758 (1999).
[43] J. P. Perdew, J. A. Chevary, S. H. Vosko, K. A. Jackson, M. R. Pederson, D. J. Singh, and C. Fiolhais, Phys. Rev. B **48**, 4978 (1993).
[44] J. P. Perdew, J. A. Chevary, S. H. Vosko, K. A. Jackson, M. R. Pederson, D. J. Singh, and C. Fiolhais, Phys. Rev. B **46**, 6671 (1992).
[45] Z. T. Y. Liu, D. Gall, and S. V. Khare, Phys. Rev. B **90**, 134102 (2014).
[46] Z. T. Y. Liu, X. Zhou, D. Gall, and S. V. Khare, Comput. Mater. Sci. **84**, 365 (2014).
[47] Z. T. Y. Liu, X. Zhou, S. V. Khare, and D. Gall, J. Phys.: Cond. Matt. **26**, 025404 (2014).
[48] J. L. Roehl, Z. T. Y. Liu, and S. V. Khare, Mater. Res. Express **1**, 025904 (2014).
[49] Y. Wang, Z. T. Y. Liu, S. V. Khare, S. Collins, J. Zhang, L. Wang, and Y. Zhao, Appl. Phys. Lett. **106**, 061906 (2016).
[50] X. Zhou, J. L. Roehl, C. Lind, and S. V. Khare, J. Phys.: Cond. Matt. **25**, 075401 (2013).
[51] I. Efthimiopoulos, J. Kemichick, X. Zhou, S. V. Khare, D. Ikuta, and Y. Wang, J. Phys. Chem. A **118**, 1713 (2014).
[52] R. Lacomba-Perales, D. Errandonea, A. Segura, J. Ruiz-Fuertes, P. Rodriguez-Hernandez, S. Radescu, J. Lopez-Solano, A. Mujica, and A. Munoz, J. Appl. Phys. **110**, 043703 (2011).
[53] V. Panchal, D. Errandonea, A. Segura, P. Rodriguez-Hernandez, A. Munoz, S. Lopez-Moreno, and M. Bettinelli, J. Appl. Phys. **110**, 043723 (2011).
[54] J. Heyd, G. E. Scuseria, and M. Ernzerhof, J. Chem. Phys. **118**, 8207 (2003).
[55] A. V. Krukau, O. A. Vydrov, A. F. Izmaylov, and G. E. Scuseria, J. Chem. Phys. **125**, 224106 (2006).
[56] P. Bruesch and F. D'Ambrogio, Phys. Stat. Sol. **50**, 513 (1972).
[57] J. Zwinscher and H. D. Lutz, J. Sol. St. Chem. **118**, 43 (1995).
[58] A. M. Hofmeister and H.-K. Mao, Proc. Natl. Acad. Sci. USA **99**, 559 (2002).
[59] H. D. Lutz, W. Becker, B. Mueller, and M. Jung, J. Ram. Spectr. **20**, 99 (1989).
[60] D. Machon, P. F. McMillan, B. Xu, and J. Dong, Phys. Rev. B **73**, 094125 (2006).
[61] A. F. Goncharov and V. V. Struzhkin, J. Raman Spectr. **34**, 532 (2003).
[62] See Supplemental Material at http://link.aps.org/supplemental/10.1103/PhysRevB.94.174106 for additional XRD spectra, detailed experimental and calculated structural data, the F-f plot and the $CdSe_4$ and $CrSe_6$ polyhedral volumes as a function of pressure for the cubic phase, the optimization process of the tetragonal c/a^* axial ratio, and the electronic densities of states for the cubic and the AFM1 and AFM2 tetragonal phases.
[63] D. Errandonea, Y. Meng, M. Somayazulu, and D. Hausermann, Phys. B **355**, 116 (2005).
[64] D. Errandonea, A. Munoz, and J. Gonzalez-Platas, J. Appl. Phys. **115**, 216101 (2014).
[65] S. Klotz, J.-C. Chervin, P. Munsch, and G. Le Marchand, J. Phys. D Appl. Phys. **42**, 075413 (2009).
[66] J. M. Besson, J. P. Itie, A. Polian, G. Weill, J. L. Mansot, and J. Gonzalez, Phys. Rev. B **44**, 4214 (1991).
[67] P. W. Stephens, J. Appl. Cryst. **32**, 281 (1999).
[68] R. B. von Dreele, J. Appl. Cryst. **30**, 517 (1997).
[69] P. G. Radaelli, New J. Phys. **7**, 53 (2005).
[70] A. Waskowska, L. Gerward, J. S. Olsen, M. Feliz, R. Llusar, L. Gracia, M. Marques, and J. M. Recio, J. Phys. Cond. Mat. **16**, 53 (2004).
[71] S. M. Sharma and S. K. Sikka, Progr. Mater. Sci. **40**, 1 (1996).
[72] W. Albers and C. J. M. Rooymans, Sol. St. Com. **3**, 417 (1965).
[73] S. D. Guo and B. G. Liu, J. Magn. Magn. Mater. **324**, 2410 (2012).
[74] I. Loa, P. Adler, A. Grzechnik, K. Syassen, U. Schwarz, M. Hanfland, G. K. Rozenberg, P. Gorodetsky, and M. P. Pasternak, Phys. Rev. Lett. **87**, 125501 (2001).
[75] J. Ruiz-Fuertes, A. Segura, F. Rodriguez, D. Errandonea, and M. N. Sanz-Ortiz, Phys. Rev. Lett. **108**, 166402 (2012).
[76] J. D. Dunitz and L. E. Orgel, J. Phys. Chem. Sol. **3**, 20 (1957).
[77] D. Errandonea, R. S. Kumar, F. J. Manjon, V. V. Ursaki, and I. M. Tiginyanu, J. Appl. Phys. **104**, 063524 (2008).
[78] C. Kant, M. Schmidt, Z. Wang, F. Mayr, V. Tsurkan, J. Deisenhofer, and A. Loidl, Phys. Rev. Lett. **108**, 177203 (2012).
[79] C. Ederer and M. Komelj, Phys. Rev. B **76**, 064409 (2007).
[80] D. Das and S. Ghosh, J. Phys. D Appl. Phys. **48**, 425001 (2015).
[81] I. Efthimiopoulos, Z. T. Liu, S. V. Khare, P. Sarin, T. Lochbiler, V. Tsurkan, A. Loidl, D. Popov, and Y. Wang, Phys. Rev. B **92**, 064108 (2015).
[82] R. D. Shannon and C. T. Prewitt, Acta Crystallogr. B **25**, 925 (1969).
[83] I. Efthimiopoulos, High-pressure structural and spectroscopic studies on transition metal compounds, Ph.D. dissertation, Aristotle University of Thessaloniki, 2010.
[84] G.-W. Chern, R. Moessner, and O. Tchernyshyov, Phys. Rev. B **78**, 144418 (2008).
[85] O. Tchernyshyov, R. Moessner, and S. L. Sondhi, Phys. Rev. Lett. **88**, 067203 (2002).
[86] Ohio Supercomputer Center, http://osc.edu/ark:/19495/f5s1ph73.